ACS APPLIED MATERIALS & INTERFACES

Research Article

www.acsami.org

Drastically Enhanced High-Rate Performance of Carbon-Coated $LiFePO_4$ Nanorods Using a Green Chemical Vapor Deposition (CVD) Method for Lithium Ion Battery: A Selective Carbon Coating Process

Ruiyuan Tian,[†] Haiqiang Liu,[†] Yi Jiang,[†] Jiankun Chen,[†] Xinghua Tan,[†] Guangyao Liu,[§] Lina Zhang,[‡] Xiaohua Gu,[‡] Yanjun Guo,[†] Hanfu Wang,*[,†] Lianfeng Sun,*[,†] and Weiguo Chu*[,†]

[†]National Center for Nanoscience and Technology of China, Beijing 100190, P. R. China

[§]China University of Geosciences, Beijing 100083, P. R. China

[‡]Department of Physics, Tsinghua University, Beijing 100084, P. R. China

Supporting Information

ABSTRACT: Application of $LiFePO_4$ (LFP) to large current power supplies is greatly hindered by its poor electrical conductivity (10^{-9} S cm^{-1}) and sluggish Li^+ transport. Carbon coating is considered to be necessary for improving its interparticle electronic conductivity and thus electrochemical performance. Here, we proposed a novel, green, low cost and controllable CVD approach using solid glucose as carbon source which can be extended to most cathode and anode materials in need of carbon coating. Hydrothermally synthesized LFP nanorods with optimized thickness of carbon coated by this recipe are shown to have superb high-rate performance, high energy, and power densities, as well as long high-rate cycle lifetime. For 200 C (18s) charge and discharge, the discharge capacity and voltage are 89.69 mAh g^{-1} and 3.030 V, respectively, and the energy and power densities are 271.80 Wh kg^{-1} and 54.36 kW kg^{-1}, respectively. The capacity retention of 93.0%, and the energy and power density retention of 93.6% after 500 cycles at 100 C were achieved. Compared to the conventional carbon coating through direct mixing with glucose (or other organic substances) followed by annealing (DMGA), the carbon phase coated using this CVD recipe is of higher quality and better uniformity. Undoubtedly, this approach enhances significantly the electrochemical performance of high power LFP and thus broadens greatly the prospect of its applications to large current power supplies such as electric and hybrid electric vehicles.

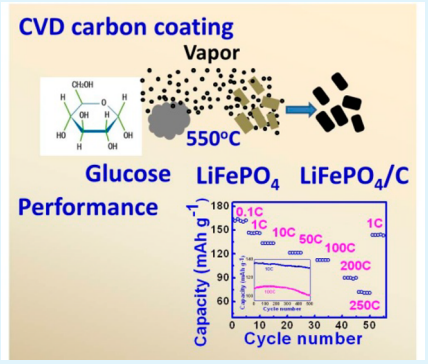

KEYWORDS: *lithium iron phosphate, CVD method, carbon coating, high-rate performance, high power density, hydrothermal method*

INTRODUCTION

Olivine-structured $LiFePO_4$ (LFP) is regarded as a very attractive candidate cathode for large scale batteries for electric and hybrid electric vehicles (EVs and HEVs) because of its low cost, environmental friendliness, high safety, high energy density (578 Wh kg^{-1}.), and long cycle lifetime since its discovery.[1−3] However, poor electronic and ionic conductivity is the greatest challenge for its practical applications in this field.[4] To address this issue, a variety of methods, such as cation doping,[5,6] surface coating, introduction of conductive agents,[7−12] and size optimization,[13,14] were attempted or combined in most cases to overcome the ionic and electronic transport limitations.

Of these methods, carbon coating is recognized as a very effective and commonly used way for improving the electronic conductivity and thus the electrochemical performance of LFP.[15−19] A uniform carbon coating of LFP with moderate thicknesses is considered to be essential for excellent rate capability and long cycle lifetime, as normally required by the application to EVs and HEVs, which however are often difficult to achieve.[20,21] At present, there are two main ways to realize the carbon coating: one is the conventional direct mixing glucose (organic substances containing carbon: sucrose etc.) with LFP followed by annealing (DMGA)[15−19] and the other is the chemical vapor deposition (CVD).[22−27] CVD is generally recognized as a simple and effective method capable of realizing uniform carbon coating as the carbon - contained vapor flows across $LiFePO_4$ to deposit carbon on its surface. In reality, according to the difference of source supplies this approach can be categorized into two types. One is to use gases, such as C_2H_4, C_2H_2, or other carbon-rich gases, mixed with H_2 or Ar as carrier and protective atmosphere, and metal salts as catalyst.[22−24] The metal salts introduced usually bring impurities, and these gases are not benign to environment and expensive. The other is to use volatile organic liquids as carbon sources, such as pyrrole monomer,[25] methylbenzene,[26] or benzene,[27] which are carried by the flow of Ar or air. The organic steams flow across $LiFePO_4$ to form conductive layers

Received: March 3, 2015
Accepted: May 13, 2015
Published: May 13, 2015

DOI: 10.1021/acsami.5b01891
ACS Appl. Mater. Interfaces 2015, 7, 11377−11386

directly[25] or carbon sources[26,27] to be carbonized subsequently. However, these volatile organic liquids are normally both toxic and expensive.

Therefore, an effective, safe, low cost and controllable CVD for uniform carbon coating is highly desired. Moreover, the availability of high quality carbon with uniform and moderate thickness would ensure sufficiently good electronic conductivity on one side and not retard the migration of Li^+ across an electrode material on the other side, which consequently makes it far more promising to explore high power LFP applicable to EVs and HEVs.

Here we developed a green, effective, low cost, and controllable CVD recipe using solid glucose as carbon source and Ar as carrier to carbon coat LFP nanorods uniformly which were hydrothermally synthesized at low temperature.[28] The carbon coated $LiFePO_4$ nanorods thus obtained are shown to have both high energy and power densities, excellent rate capability and long cycle lifetime even at very high charge and discharge rates such as 100 C (1 C = 170 mA g^{-1}). By controlling the weight percentage of coated carbon the electrochemical performance of LFP was optimized, which was drastically enhanced compared to the optimized performance of LFP carbon coated through the conventional DMGA. The influence of the carbon weight percentage on the structure and electrochemical performance of LFP nanorods is discussed in detail.

EXPERIMENTAL SECTION

Synthesis of Carbon-Coated $LiFePO_4$ Nanorods. $LiFePO_4$ nanorods were hydrothermally synthesized at low temperature using tetraglycol as surfactant in which the mixture of tetraglycol and deionized water (80/20, v/v) was used as a reaction medium. The details can be found in ref 28. The preparation process of carbon coated LFP nanorods is schematically illustrated in Figure 1. From

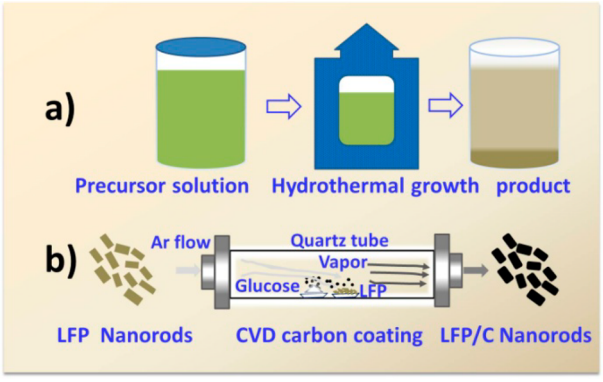

Figure 1. Schematic illustration of the preparation process of carbon coated LFP nanorods. Hydrothermal synthesis (a) and carbon coating using a CVD method (b).

Figure 1b the carbon coating using the CVD recipe was carried out in a quartz tube horizontally located in the furnace. The crucible with glucose powder as carbon source was placed upstream close to the crucible with hydrothermally synthesized LFP (labeled by sample H). The quartz tube was heated up to 550 °C at a rate of 10 °C min^{-1} and maintained for 1 h in an Ar flow of 200 cm^3 min^{-1}. The furnace was cooled down naturally with the Ar flow. The weight ratios of 1:1, 2:1, and 4:1 for glucose to bare LFP nanorods (labeled by C-1, C-2, and C-3, respectively) were attempted to explore the influence of carbon content on the structure and electrochemical performance. In addition, the direct mixtures of hydrothermally synthesized LFP nanorods with glucose in different weight ratios were also treated under the same conditions above, and an optimum glucose weight percentage, 15 wt % (labeled by sample G-15) was obtained.

Structural Characterization. The structure, morphology, carbon content, and properties of the above samples were studied using X-ray diffraction (XRD, Rigaku 2400, Rigaku company, Japan), scanning electronic microscopy (SEM, NanoSEM 430, FEI company, USA), transmission electronic microscopy (TEM), high resolution transmission electronic microscopy (HRTEM, Tecnai G2 F20 S-Twin, FEI company, USA), carbon and sulfur analysis (CSA, CS-344, LECO Company, USA), and Raman spectra (Renishaw Invia, UK), respectively. The XRD data were collected with a Cu Kα radiation at 50 kV and 200 mA. The data for Rietveld refinements were recorded from 15° to 130° with a step size of 0.02°, and a step time of 2s.

Nitrogen adsorption/desorption isotherms were acquired at 77 K using a Micromeritics TriStar II 3020 instrument (USA). Specific surface areas and cumulative pore volumes of LFP were calculated by the Brunauer–Emmet–Teller (BET) and the density functional theory (DFT) methods, respectively. To evaluate the quality of coated carbon for samples C-2 and G-15 micro-Raman spectra were acquired at room temperature with a laser beam size of about 1 μm, an argon ion laser operating at 632.8 nm and a resolution of 1 cm^{-1}.

Electrochemical Measurements. The active material, acetylene black and polyvinylidene fluoride (PVDF) with a weight ratio of 70:20:10 were mixed with *N*-methyl-2-pyrrolidinone (NMP) as the solvent. The resulting slurry was pasted on an aluminum foil and dried under vacuum at 100 °C for 12h, which then was punched into circular cathode and pressed under 20 MPa. The loading density is about 2.0 mg cm^{-2}. The CR 2025 coin cells were assembled in an Ar-filled glovebox with a lithium metal as counter electrode and Celgard 2316 as a separator. The electrolyte was 1 mol/L LiPF6 dissolved in a mixture of EC ethylene carbonate (EC), ethyl methyl carbonate (EMC), and dimethyl carbonate (DMC) with a volume ratio of 1:1:1. Electrochemical measurements were carried out on a battery test system (BTS, 5 V; Neware Company, China) at room temperature (25 °C). The same rates were employed for both charge and discharge. Electrochemical impedance spectra (EIS) were collected using an electrochemical workstation (CHI660D, Shanghai Chenghua Company, China).

RESULTS AND DISCUSSION

The XRD patterns of samples H, C-1, C-2, C-3, and G-15 are presented in Figure 2. All the samples show very similar patterns in which the reflections can be identified as $LiFePO_4$ except for some minor impurities in sample H. Compared to samples C-1, C-2, C-3, and G-15 with comparable reflection intensities the reflections for sample H are weaker, which could be ascribed to its relatively poorer crystallinity due to lack of annealing upon carbon coating. To obtain the details of their

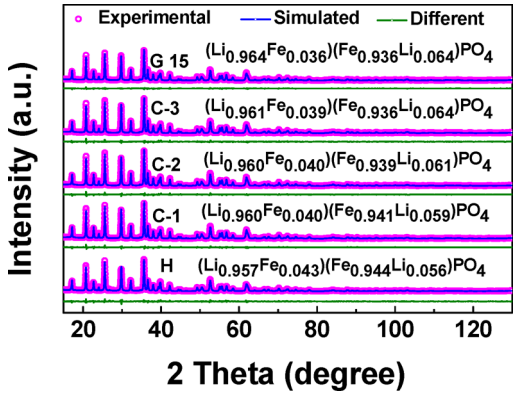

Figure 2. Experimental, simulated and different XRD patterns of samples H, C-1, C-2, C-3, and G-15.

DOI: 10.1021/acsami.5b01891
ACS Appl. Mater. Interfaces 2015, 7, 11377–11386

Table 1. Refined Parameters for Samples H, C-1, C-2, C-3, and G-15

parameters		H	C-1	C-2	C-3	G-15
a (Å)		10.3143	10.3080	10.3091	10.3084	10.3116
b (Å)		5.9884	5.9951	5.9954	5.9954	5.9989
c (Å)		4.6991	4.6929	4.6939	4.6928	4.6942
crystallite size	200	56.5	67.5	68.6	64.6	60.5
	101	89.7	103.0	107.1	102.9	94.1
	020	44.4	70.0	64.2	66.4	71.9
reliability factors	R_{wp}	12.8%	11.3%	11.1%	11.1%	11.3%
	R_B	3.055%	3.119%	3.010%	2.960%	3.252%
	S	1.749	1.587	1.552	1.552	1.044
refined formula		$(Li_{0.957}Fe_{0.043})(Fe_{0.944}Li_{0.056})PO_4$ $Li_{1.013}Fe_{0.987}PO_4$	$(Li_{0.960}Fe_{0.040})(Fe_{0.941}Li_{0.059})PO_4$ $Li_{1.019}Fe_{0.981}PO_4$	$(Li_{0.960}Fe_{0.040})(Fe_{0.939}Li_{0.061})PO_4$ $Li_{1.021}Fe_{0.979}PO_4$	$(Li_{0.961}Fe_{0.039})(Fe_{0.936}Li_{0.064})PO_4$ $Li_{1.025}Fe_{0.975}PO_4$	$(Li_{0.964}Fe_{0.036})(Fe_{0.936}Li_{0.064})PO_4$ $Li_{1.028}Fe_{0.972}PO_4$
impurities		−2.46%				

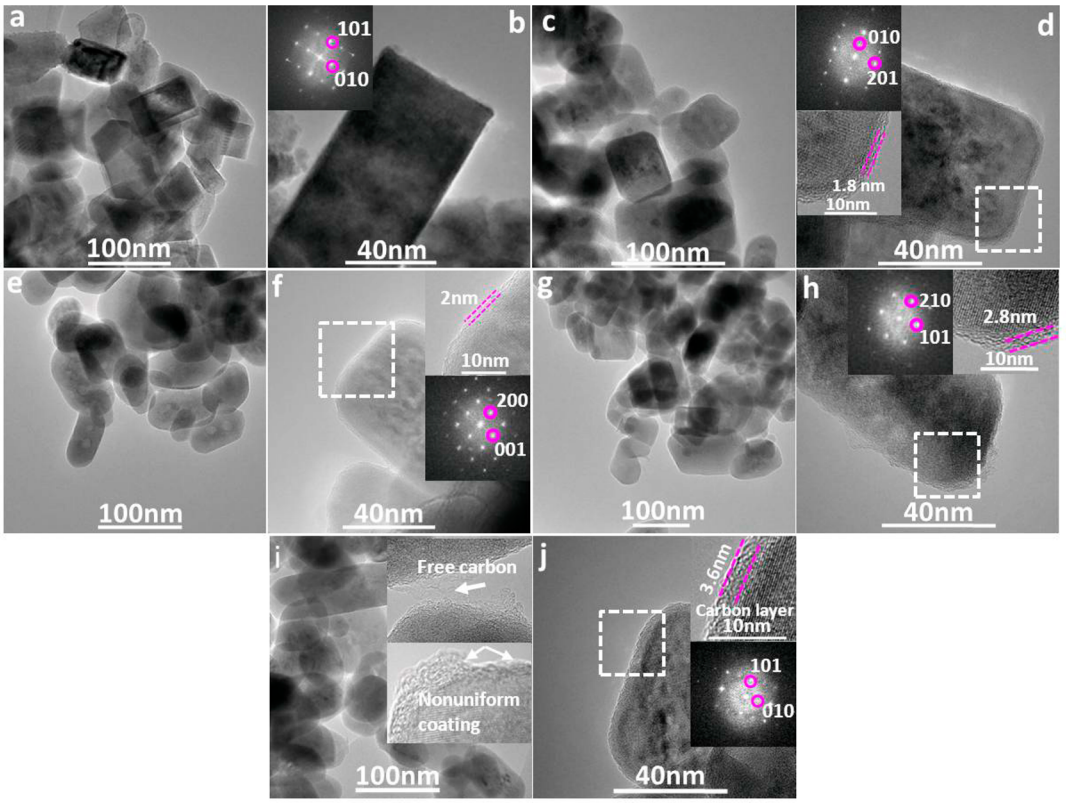

Figure 3. TEM (a, c, e, g, i), HRTEM images (b, d, f, h, j), and their corresponding FFT of samples H, C-1, C-2, C-3, and G-15. LFP is rod-like and one short axis is along [010], favoring the Li^+ diffusion. Note different thicknesses of carbon layers and carbon distribution.

structures, we performed Rietveld refinements on the XRD data using an orthorhombic structure model with space group of *Pnma*.[29] Their experimental and simulated patterns are found to agree very well. The refined parameters are outlined in Table 1 from which one can see a lattice contraction along both a and c but an expansion along b after carbon coating through CVD. This change was also observed for the samples carbon coated through DMGA.[28] The sizes along the directions normal to (200), (101), and (020) were estimated according to the Scherrer equation,[30] suggesting a rod-like morphology.[28] After carbon coating the size of nanorods for all samples tends to increase with a decreased aspect ratio. However, the sharp corners of bare LFP nanorods appear to be spheroidized due to carbon coating, which will be shown by the following TEM images. The changes occurring in morphology and size of LFP subject to carbon coating through CVD and DMGA are quite similar. Upon Rietveld refinements the occupancies of Li at the Fe site and of Fe at the Li site were refined as well. Thus, the refined formulas could be derived to be $(Li_{0.957}Fe_{0.043})$-$(Fe_{0.944}Li_{0.056})PO_4$ $(Li_{1.013}Fe_{0.987}PO_4)$, $(Li_{0.960}Fe_{0.040})$-$(Fe_{0.941}Li_{0.059})PO_4$ $(Li_{1.019}Fe_{0.981}PO_4)$, $(Li_{0.960}Fe_{0.040})$-$(Fe_{0.939}Li_{0.061})PO_4$ $(Li_{1.021}Fe_{0.979}PO_4)$, $(Li_{0.961}Fe_{0.039})$-$(Fe_{0.936}Li_{0.064})PO_4$ $(Li_{1.025}Fe_{0.975}PO_4)$, and $(Li_{0.964}Fe_{0.036})(Fe_{0.936}Li_{0.064})PO_4$ $(Li_{1.028}Fe_{0.972}PO_4)$ for samples H, C-1, C-2, C-3, and G-15, respectively. The Li site is found to be occupied by around 4% Fe and the Fe site by around 6% Li for all samples, also consistent with the results reported in ref 28. All of this clearly reveals that differing carbon coatings had little influence on the size, morphology and crystal structure of LFP.

TEM, HRTEM images, and their corresponding fast Fourier transformation (FFT) for these samples are shown in Figure 3. TEM observations show a rod-like morphology as well, in accordance with the XRD results. The combination of HRTEM

DOI: 10.1021/acsami.5b01891
ACS Appl. Mater. Interfaces 2015, 7, 11377−11386

and corresponding FFT allows one to conclude that one short axis is along [010], which would undoubtedly favor the migration of Li^+.[31−34] Close inspection reveals that LFP nanorods were uniformly coated with carbon layers with different thicknesses for samples C-1, C-2, and C-3. By comparing Figure 3 d, f and h, with the increased weight ratio of glucose to bare LFP the thickness tends to increase from 1.8 nm through 2.0 to 2.8 nm, consistent with the increased weight percentages of carbon as determined by the CSA, such as 2.25 wt % for sample C-1, 2.35 wt % for sample C-2, and 3.09 wt % for sample C-3. In sharp contrast, some free carbon and nonuniform coatings were observed for sample G-15 with a weight percentage of 3.40% through lots of LFP nanorods inspection, and even carbon layer as thick as 3.6 nm was seen, as shown in Figure 3i and j. Though the carbon coating is not uniform for sample G-15 the thickness of carbon layer tends to increase with increased weight percentage of coated carbon. For the hydrothermally synthesized bare LFP there is no carbon layer at the surface of LFP nanorods, as shown in Figure 3b. As far as the more macroscopic scale is concerned, the morphologies for those samples are quite similar and uniform, as shown in Figure S1 (Supporting Information).

Nitrogen adsorption/desorption isotherm measurements were carried out to further investigate the size of pores involved in the samples. Their isotherms and curves of cumulative pore volume versus pore size are shown in Figure 4. It can be found from Figure 4 a that the isotherms of samples

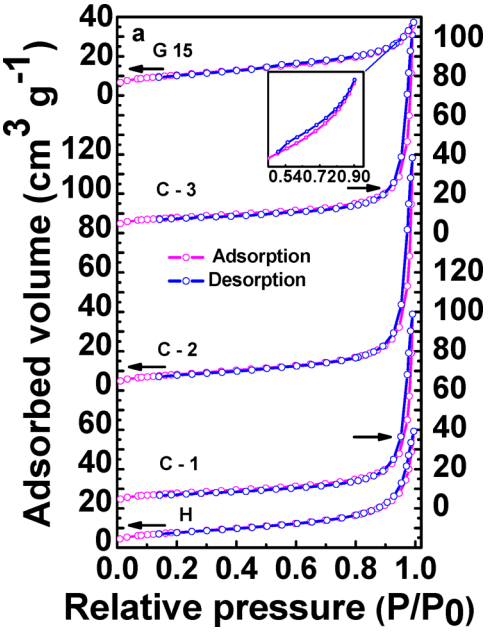

Figure 4. Nitrogen adsorption/desorption isotherms (a) and cumulative pore volumes versus pore size (b) of samples H, C-1, C-2, C-3, and G-15.

H, C-1, C-2, and C-3 are different from that for sample G-15. The formers have a hysteresis loop with P/P_0 spanning between 0.9 and 1.0 and the latter has one with P/P_0 between 0.5 and 0.8 shown in the inset. Therefore, the formers' isotherms imply the presence of very large pores and/or the simple aggregation and packing of LFP nanoparticles whereas the latter's one suggests the presence of some meso- and macropores.[35−38] Indeed, Figure 4 b shows that a faster volume increase of pores smaller than 20 nm takes place for sample G-15 and the increasing rates of the volumes of pores below 20 nm for samples H, C-1, C-2, and C-3 are slow and almost same, whereas the volume of pores larger than 20 nm for sample H increases even more slowly. The BET surface areas for samples H, C-1, C-2, C-3, and G-15 are 27.91, 27.39, 29.36, 28.46, and 31.04 $m^2\ g^{-1}$, respectively. On the basis of the sizes of LFP nanorods in Table 1 their corresponding BET surface areas were figured out to be 28.54, 21.56, 21.94, 22.37, and 22.81 $m^2\ g^{-1}$, respectively. The calculated (28.54 $m^2\ g^{-1}$) and measured (27.91 $m^2\ g^{-1}$) BET surface areas for sample H are found to agree well. However, the calculated ones for the carbon coated samples are all smaller than the measured ones, obviously, which can be ascribed to their carbon coatings. On one side, the size increase of LFP nanorods after carbon coating results in a decrease of the BET surface area, on the other side the introduction of pores smaller than LFP nanorods leads to its increase. Thus, the BET surface areas for the carbon coated samples resulted from the competition between the two opposite effects in which, therefore, the incorporation of smaller pores for sample G-15 carbon coated through DMGA led to a higher surface area.

To gain further insights into the coated carbon the typical micro-Raman spectra for samples C-2 and G-15 are shown in Figure 5. Samples C-1 and C-3 exhibit spectra similar to those of sample C-2 which are therefore not presented. For each sample we acquired eight spectra at eight different points selected randomly in which one of them is given in Figure 5 and the others are given in Figure S2 (Supporting Information). Because of the strong effect of the resonant enhancement of the carbon coating, its Raman bands dominate

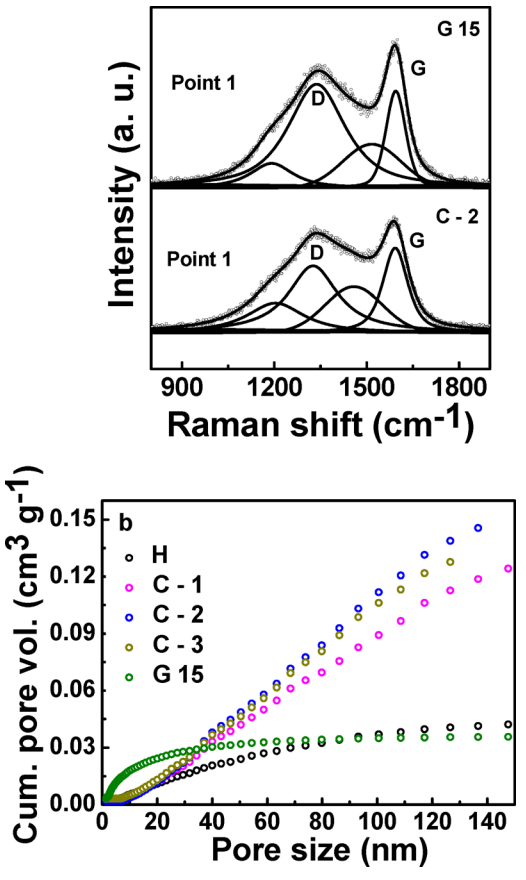

Figure 5. Raman spectra of samples C-2 and G-15.

DOI: 10.1021/acsami.5b01891
ACS Appl. Mater. Interfaces 2015, 7, 11377−11386

Table 2. Parameters of the D- and G-Band Fitted Using the Four Gaussian−Lorentzian Bands Spectra Recorded at Different Points of Samples C-2 and G-15[a]

samples	parameters		point 1	point 2	point 3	point 4	point 5	point 6	point 7	point 8
C-2	band position (cm^{-1})	D	1325.69	1332.00	1330.92	1334.28	1331.32	1326.69	1329.69	1332.05
		G	1592.58	1590.01	1592.82	1590.84	1592.34	1591.21	1593.14	1594.71
	FWHF (cm^{-1})	D	193.77	195.17	190.67	176.95	184.77	180.81	210.79	183.98
		G	96.49	95.43	95.61	88.33	93.40	98.20	94.79	90.68
	intensity (a.u.)	D	280996	1896330	733063	1007130	1484980	421197	369376	275216
		G	157469	1019460	493188	566183	1007580	355441	182644	167207
	I_D/I_G		1.78	1.86	1.49	1.78	1.47	1.19	2.02	1.65
	L_{ab} (nm)		4.64	4.45	5.57	4.66	5.62	6.99	4.10	5.03
G-15	band position (cm^{-1})	D	1337.48	1336.81	1337.65	1338.15	1339.22	1337.39	1343.33	1333.71
		G	1594.37	1590.65	1589.58	1589.53	1594.67	1595.01	1593.65	1592.99
	FWHF (cm^{-1})	D	221.69	194.97	192.48	183.53	183.89	235.04	173.54	199.37
		G	75.98	76.45	74.62	74.22	80.15	78.95	82.58	72.97
	intensity (a.u.)	D	464577	2248340	2039900	1787210	386666	354327	237646	702918
		G	125051	715385	528415	514862	155184	101335	125255	214105
	I_D/I_G		3.72	3.14	3.86	3.47	2.49	3.50	1.90	3.28
	L_{ab} (nm)		2.23	2.64	2.15	2.39	3.32	2.37	4.37	2.52

[a]Those spectra are reported in Figure 5 and Supporting Information Figure S2.

over the bands of LFP.[39,40] To analyze the nature of the bands associated with carbon, the experimental spectra were fitted by combining four Gaussian−Lorentzian bands. After determining the baselines the fittings of the bands were carried out by refining their full widths at half height (fwhm), positions and intensities, as outlined in Table 2. The bands at around 1330 and 1590 cm^{-1} are the characteristic bands of carbon assigned to the D- and G-bands, respectively.[41,42] The bands at around 1200 and 1500 cm^{-1} are considered to arise from poorly organized carbon materials and defects outside the plane of aromatic layers.[43−45] The intensity ratio of the D- to G-band, $R(\lambda_L = I_D/I_G)$ related to a laser excitation wavelength, gives important information on the nature of carbon phase. For crystalline graphite simply the G-band is present. In fact, $R(\lambda_L)$ can be related to an in plane correlation length L_{ab}, which quantifies the mean basal plane diameter of graphite parallel to (001) through a modified Tuinstra−Koenig relation $L_{ab} = C(\lambda_L)/R(\lambda_L)$ ($400 < \lambda_L < 700$ nm).[46,47] $C(\lambda_L)$ is correlated to the exciting wavelength through $C(\lambda_L) = C_0 + \lambda_L C_1$ with $C_0 = -12.6$ nm and $C_1 = 0.033$.[46,47] $R(\lambda_L)$ was calculated to be from 1.19 to 2.02 and thus 4.10 nm $\leq L_{ab} \leq$ 6.99 nm for sample C-2, and from 1.9 to 3.86 and thus 2.1 nm $\leq L_{ab} \leq$ 4.37 nm for sample G-15. This clearly suggests that the coated carbon for sample G-15 was more disordered than that for sample C-2. As a consequence, the carbon coated using the CVD recipe reasonably has a better electronic conductivity than that through DMGA, which would expected to have a different effect on the electrochemical performance of samples.

To investigate the influences of the ratio of glucose to bare LFP and of the coating way on the rate performance, rate capability and discharge curves of samples C-1, C-2, C-3, and G-15 at different rates are displayed in Figure 6 and Supporting Information Figure S3, respectively. All samples show quite similar discharge capacities at 0.1 C, such as 161.32, 161.76, 161.63, and 163.85 mAh g^{-1} for samples C-1, C-2, C-3, and G-15, respectively. However, the rate capability of these samples increasingly differs with increased rates. At the rate of 1 C, sample G-15 shows lower capacity compared to other samples. From 50 C on, obviously poorer rate capability was observed for sample C-3. At 80 C, sample C-1 also begins to have a lower discharge capacity than that of sample C-2. Nevertheless, all the

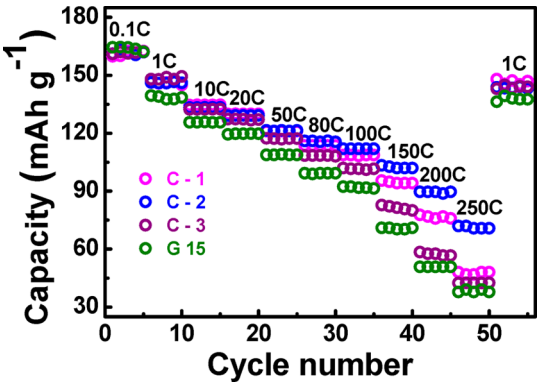

Figure 6. Rate performance of samples C-1, C-2, C-3, and G-15.

samples have quite superior high rate performance. At 100 C, samples C-1, C-2, C-3, and G-15 have capacities of 108. 64, 111.95, 101.55, and 91.96 mAh g^{-1}, respectively, and still retain capacities of 47.54, 71.27, 42.48, and 38.35 mAh g^{-1}, respectively, with the rate up to 250 C. So superior high-rate performance with a percentage of carbon black additive as low as 20% is of great practical significance to the application of LFP to large current power supplies, such as EVs and HEVs, which is the very goal for researchers to keep pursuing.[20,21] More importantly, the discharge curves with well-defined voltage plateaus for these samples even at very high rates still are characterized by a typical Li^+ insertion dominated process instead of a Li^+ accumulation process at the surface being of a capacitor-like behavior which LFP usually performs at high rates, as shown in Supporting Information Figure S3.[48] This is extremely important for its practical use as power supplies of large current.

To gain further insight into the electrochemical performance of these samples, their voltages at 50% depth of discharge (DOD), polarizations, power, and energy densities are shown in Figure 7. Samples C-1, C-2, C-3, and G-15 exhibit quite small polarizations of 13.0, 12.3, 11.6, and 14.0 mV at 0.1 C, respectively, and very high discharge voltages of 2.886, 2.965, 2.906, and 2.880 V at the rate of 250 C, respectively. Sample C-2 has the highest energy and power densities, such as 358.45

DOI: 10.1021/acsami.5b01891
ACS Appl. Mater. Interfaces 2015, 7, 11377−11386

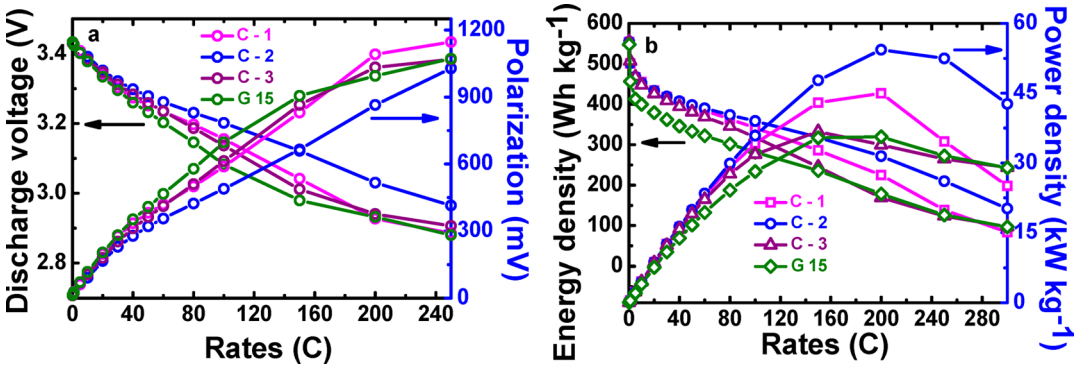

Figure 7. Polarizations, discharge voltages at 50% DOD (a), power and energy densities versus C rates for samples C-1, C-2, C-3, and G-15 (b).

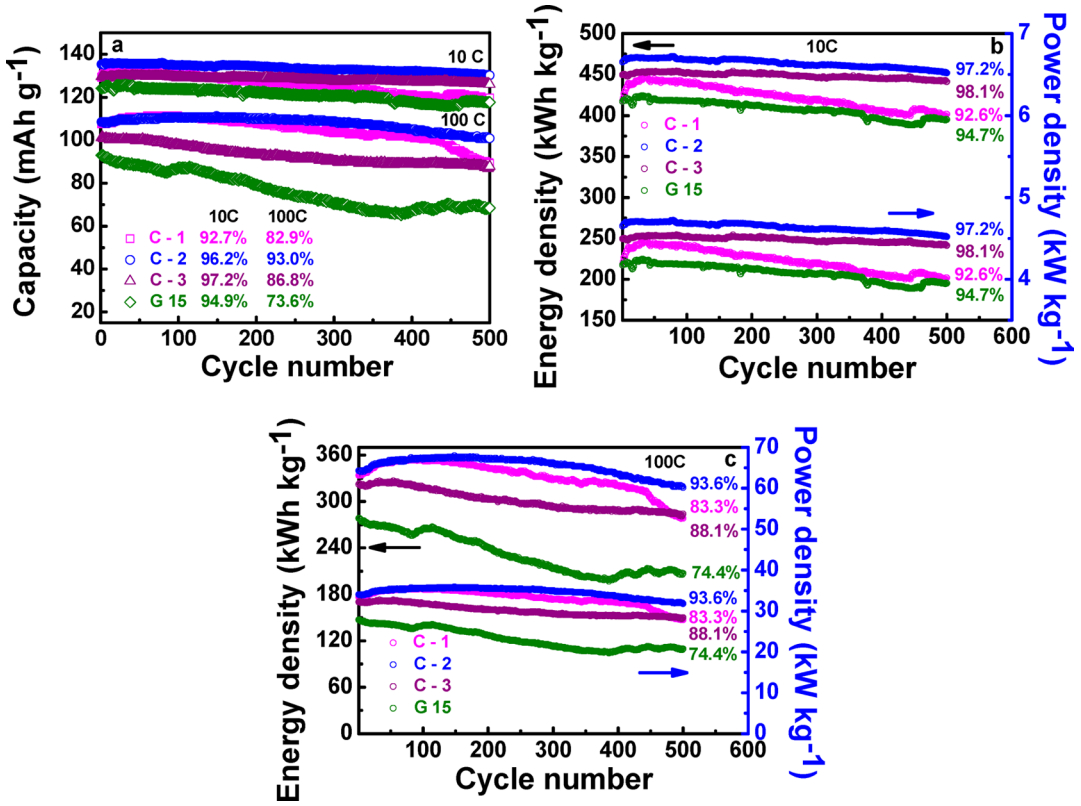

Figure 8. Cycling performance of discharge capacity (a), power and energy densities for the rates of 10 C (b) and 100 C (c) for samples C-1, C-2, C-3, and G-15.

Wh kg^{-1} and 35.85 kW kg^{-1} for 100 C, and 271.80 Wh kg^{-1} and 54.36 kW kg^{-1} for 200 C, which are quite fascinating for its practical applications to the large current field. Small polarizations are normally the prerequisite that cathode materials have good electrochemical performance. The very small polarizations, the very high discharge voltages and the very high energy and power densities for sample C-2 with a low percentage of carbon black additive particularly at high rates here are extremely outstanding among the literature.[34,49−52] In contrast, sample G-15 has the worst performance, which however still is quite good compared to the literature.[53,54]

Cycle lifetime is a very crucial parameter for evaluating the performance of a cathode material, which is extremely important for applications to EVs and HEVs. Therefore, the cycling tests of samples C-1, C-2, C-3, and G-15 at the rates of 10 and 100 C at room temperature were carried out. The dependences of their discharge capacities, energy and power densities on cycle numbers are shown in Figure 8. Their capacity retentions after 500 cycles are 92.7%, 96.2%, 97.2%, and 94.9% for 10 C respectively, and 82.9%, 93.0%, 86.8%, and 73.6% for 100 C, respectively. More importantly, their energy and power density retentions after 500 cycles are 92.6%, 97.2%, 98.1%, and 94.7% for 10 C, respectively, and 83.3%, 93.6%, 88.1%, and 74.4% for 100C, respectively which are even higher than their corresponding capacity retentions. The energy and power density retention actually is a more rigorous evaluation of the cycling performance of a cathode material as it reflects a change of the product of discharge capacity and voltage against cycle number. Sample C-2 has the highest energy and power density retention after 500 cycles for the rate as high as 100 C (36 s), which is indeed exciting for its application to large current power supplies. Though sample G-15 shows the lowest energy and power density retention at 100 C, it is still quite good. Due to the unavailability of the cycling performance at

DOI: 10.1021/acsami.5b01891
ACS Appl. Mater. Interfaces 2015, 7, 11377−11386

high rates, such as 100 C, it is quite difficult to make comparison to the literature. However, these retentions after 500 cycles at 10 C for all the samples are very high compared to the reported ones.[51,52]

To estimate the resistances of samples C-1, C-2, C-3, and G-15, their EIS were acquired in Figure 9. The parameters derived

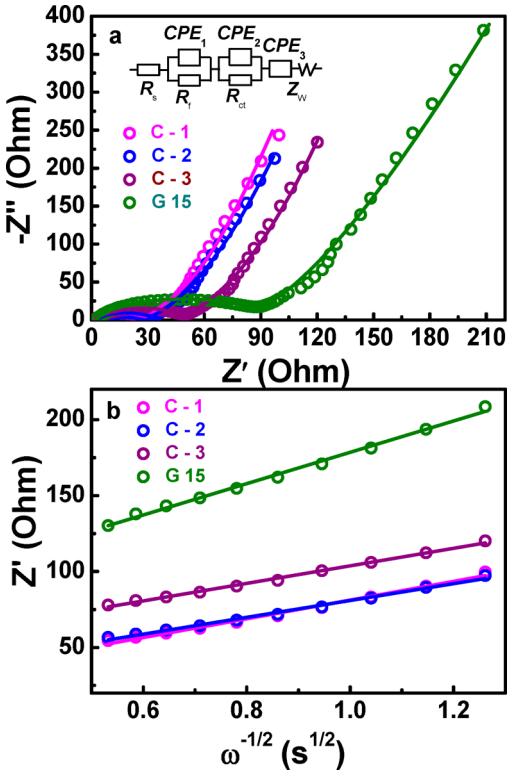

Figure 9. Experimental and simulated impedance spectra of samples C-1, C-2, C-3, and G-15 (a) and the relationships between the impedances versus $\omega^{-1/2}$ (b).

from the equivalent model proposed in Figure 9a and the diffusion coefficients of Li^+ calculated from the relationships between the resistances versus $\omega^{-1/2}$ in Figure 9b are given in Table 3. In the model, R_s is the resistance of the electrolyte and

Table 3. Resistances Derived from EIS-Based on the Proposed Circuit Model and the Diffusion Coefficients of Li^+ for Samples C-1, C-2, C-3, and G-15

sample	R_s (Ω)	R_f (Ω)	R_{ct} (Ω)	D (cm^2 s^{-1})
C-1	1.57	26.37	11.10	1.82×10^{-14}
C-2	2.82	12.54	13.30	2.25×10^{-14}
C-3	1.87	5.89	37.81	2.07×10^{-14}
G-15	2.39	50.64	29.22	0.65×10^{-14}

electrode, R_f and R_{ct} are the resistances of the films and the charge transfer, CPEs are the capacities, and Z_w is the Warburg impedance. Samples C-1 and C-3 have the lowest and highest charge transfer resistances, respectively, and samples C-3 and G-15 have the lowest and highest film resistances, respectively, as outlined in Table 3. Sample C-2 has the lower resistances of both the films and charge transfer. The diffusion coefficients of Li^+ for samples C-1, C-2, C-3, and G-15 are 1.82×10^{-14}, 2.25×10^{-14}, 2.07×10^{-14}, and 0.65×10^{-14} cm^2 s^{-1}, respectively, which seem to be dependent on the resistances of both the films and charge transfer and are comparable to the values reported.[55−57] The diffusion coefficient of Li^+ decreases in the sequence of samples C-2, C-1, C-3, and G-15, and the rate performance shows the same change sequence. This implies that the rate performance is closely related to the diffusion kinetics of Li^+ in the sample. However, the cycling performance appears not to be directly dependent on the diffusion coefficient of Li^+.

One should bear in mind that the diffusion coefficient of Li^+ for sample C-2 with excellent high rate performance was not higher than but comparable to other normally reported values, as pointed out above. At 200 C (theoretically 18 s), the discharge capacity was about 90 mAh g^{-1}, which corresponds to a real discharge duration of about 9.5 s. If it is reasonably assumed that at very high rates Li^+ insertion/deintercalation occurred mostly across the outermost layer of LFP in which the layer thickness is dependent on the real discharge capacity and the length along [010]. For 90 mAh g^{-1} and 64.2 nm along [010] shown in Table 1, the layer thickness for 90 mAh g^{-1} capacity is about 10 nm, whose discharge duration can be calculated to be about 44.4 s based on the measured diffusion coefficient of Li^+, 2.25×10^{-14} cm^2 s^{-1}. Thus, a relatively large discrepancy was found between the real (9.5 s) and theoretical (44.4 s) discharge durations. This discrepancy may arise from the following facts. First, several methods could be used for the determination of diffusion coefficient of Li^+, and it is hard to justify which result is true. Normally the diffusion coefficients of Li^+ for LFP (usually determined in the state not subject to charge or discharge) based on EIS data span a wide range regardless of whether or not LFP has very good rate capability.[51,59,60] However, EIS is a quite popular method for the determination of diffusion coefficient of Li^+ and thus it is reliable to make a comparison on Li^+ diffusion coefficients for different samples under the similar measurement conditions. Second, the diffusion coefficient of Li^+ usually varies with discharge and charge depths,[61] and the ionic conductivity is usually better upon partial charge and discharge. Finally, LFP is considered to undergo two kinds of phase transitions dependent on different charge or discharge rates. For low charge or discharge rates a two phase transition takes place and for high charge or discharge rates a solid solution phase transition occurs.[62] The migration behavior of Li^+ may be significantly influenced by the modes of phase transition as well. Therefore, in this case it may be questionable to use the diffusion efficient of Li^+ to calculate the migration time of Li^+ with certain particle sizes. In fact, there are some cases that high rate capability could not be well explained in terms of the calculated time based on the diffusion coefficient of Li^+.[51,59,60] In reality, for LFP there are still lots of things to be unveiled, such as kinetics related phase transition, especially in the cases of very high rate charge and discharge. Much care should be taken to assess the high rate performance of LFP based on the measured diffusion coefficient of Li^+.

Carbon coating has been recognized as an indispensible process for LFP and some other cathode materials to improve their electronic conductivity and furthermore their electrochemical performance.[15−19] The quality, distribution, uniformity, and thickness of carbon closely related to its coating way has a significant influence on the electrochemical performance of cathode materials.[58,63,64] In this study, the CVD approach using glucose as carbon source has been successfully applied to the carbon coating of LFP nanorods, and their performance was significantly improved. A combination of

DOI: 10.1021/acsami.5b01891
ACS Appl. Mater. Interfaces 2015, 7, 11377−11386

TEM, HRTEM, Raman spectroscopy, and carbon weight determination above revealed that samples C-1, C-2, and C-3 were uniformly coated with high quality carbon with increased thickness and weight percentage. In sharp contrast, sample G-15 through DMGA was nonuniformly coated with relatively poor quality carbon with an optimized weight percentage. The electrochemical performance of LFP is sensitive to the quality, uniformity and thickness of carbon layer.

Sample C-2 has the best rate and cycling performance due to the high quality, moderate and uniform thickness of coated carbon. However, sample G-15 exhibits the worst rate performance on account of the relatively poor quality and nonuniform thickness of carbon. For the low rates (say 20 C) samples C-1, C-2, and C-3 have both good enough electronic and ionic conductivity and thus have the almost same rate performance. With the rate up to 50 C sample C-3 with good enough electronic conductivity begins to perform somewhat poorly compared to sample C-2 because of its thicker carbon layer retarding the insertion/extraction kinetics of Li^+, which results in a higher charge transfer resistance, as shown in Table 3.[55] With a further increase of rate up to 100 C the rate performance of sample C-1 also starts to get poorer due to its slightly thinner carbon layer responsible for the insufficiently good interparticle electronic conductivity.[55] The cycling performance of samples appears to be more dependent on their electronic conductivities, especially for the low rate (say 10 C) with fast enough Li^+ migration, as shown in Figure 8. The unsteady changes of capacity, energy and power densities with increased cycle number for sample G-15 are probably related to the nonuniform distribution of carbon, as observed by TEM and HRTEM.

Different processes of carbon coating resulting in the different quality and distribution of carbon are readily understandable. For the CVD approach when glucose is heated to 550 °C it becomes a fluid in the state of liquid or semi−solid. At this temperature, the substance containing carbon and hydrogen can be evaporated to flow with argon to reach the surface of LFP nanorods in the downstream where the vapor would condense in the form of very small clusters composed of carbon or carbon and hydrogen, as shown in Figure 1.[65] With the evaporation going on the carbon layers gradually form and get thicker and thicker uniformly. Certainly, the higher the ratio of glucose to bare LFP, the higher the concentration of vapor in a constant volume of space and with a constant argon flow is, the thicker the coated carbon layer within the same duration gets. Therefore, it is reasonable that the weight percentage and thickness of coated carbon increases in the sequence of samples C-1, C-2, and C-3 with the increased weight ratios of glucose to bare LFP, 1:1, 2:1, and 4:1. More importantly, the evaporation is equivalent to a process of selection, that is, the more active molecules containing carbon or carbon and hydrogen with weak interactions to their surrounding can preferentially escape from the local environment to form the vapor. These selected molecules can condense on the surface of LFP nanorods to form the high quality carbon phase. For the conventional DMGA at 550 °C it is difficult for the glucose fluid in the state of liquid or semisolid to form uniform layers over LFP nanorods. To the contrary of the above CVD process, some molecules with weak interactions to glucose are also evaporated to form vapor to be taken away by the flow of argon. Thus, the residues of glucose after evaporation would form the relatively poor quality carbon phase on the surface of or in between LFP nanorods. Therefore, it is natural to observe some free carbon in between LFP nanorods shown in Figure 3i for sample G-15. In a word, the essential difference for the CVD and DMGA approaches is that the vapor from glucose forms the carbon phase for the former, whereas the residues of glucose after evaporation are carbonized for the latter.

Here, we should point out that the weight percentage of acetylene black conductive agent for high-rate performance tests is 20%, higher than normal weight percentage, 10% or 15%. However, in sharp contrast, the weight percentages of conductive agents used for high rate capability tests were even much higher in other reports, such as 35% or even 65%.[34,50] In fact, we also tried 10, 15, and 30 wt % conductive agents and found that the addition of 30 wt % acetylene black did not cause a significant improvement in high rate performance for sample C-2. Consequently, 20 wt % conductive additive used in this study was enough to ensure the sufficiently good electronic conductivity between particles and thus to allow LFP to perform very well. This also evidenced the good electronic conductivity resulting from CVD carbon coating.

To sum up, samples C-1, C-2, C-3, and G-15 show excellent rate performance and high rate cycling performance due to good enough intraparticle electronic conductivity (Fe^{2+} replaced partly by Li^+),[28] small size along [010] and good interparticle electronic conductivity as a result of carbon coating. The more superior electrochemical performance for sample C-2 can be ascribed to the higher quality, more uniform and moderate thickness of carbon layer coated by the CVD approach. Then, it opens up a way to enhance the electrochemical performance of $LiFePO_4$ by controlling the synthesis recipes to suppress the occupation of Fe at the Li site and maintain the moderate occupation of Li at the Fe site.

CONCLUSION

A novel, green, low cost and controllable CVD carbon coating approach using solid glucose as source was proposed. The coated carbon layer using this recipe is of higher quality and more uniform thickness compared to the conventional method through direct mixing with glucose (organic substances) followed by annealing (DMGA). This approach is universal which can be extended to most cathode and anode materials in need of coating carbon. The hydrothermally synthesized LFP nanorods carbon coated using this recipe show very small polarizations, superb rate performance, long high-rate cycling lifetime, and very high energy and power densities. The electrochemical performance of carbon coated LFP nanorods is quite sensitive to the weight percentage and thus thickness of carbon layer. The thickness-optimized sample has a discharge capacity of 71.98 mAh g^{-1} and a discharge voltage of 2.965 V for the charge and discharge rate of 250 C (14.4s). Energy and power densities as high as 358.45Wh kg^{-1} and 35.85 kW kg^{-1} at 100 C, as well as 271.80 Wh kg^{-1} and 54.36 kW kg^{-1} at 200 C, were achieved. High capacity retentions of 96.2% and 93.0%, and energy and power density retentions of 97.2% and 93.6% after 500 cycles for 10 and 100 C, respectively were obtained. This work will bring greater promise for high power $LiFePO_4$ to be applied to large current demands, especially electric and hybrid electric vehicles.

ASSOCIATED CONTENT

Supporting Information

Figure S1, SEM images of samples H (a), C-1 (b), C-2 (c), C-3 (d), and G-15 (e); Figure S2, experimental Raman spectra and the fitted spectra using four Gaussian−Lorentzian bands at

DOI: 10.1021/acsami.5b01891
ACS Appl. Mater. Interfaces 2015, 7, 11377−11386

different points for samples C-2 and G-15; and Figure S3, discharge curves at different rates for samples C-1, C-2, C-3, and G-15. The Supporting Information is available free of charge on the ACS Publications website at DOI: 10.1021/acsami.5b01891.

AUTHOR INFORMATION

Corresponding Authors

*E-mail: wanghf@nanoctr.cn
*E-mail: sunlf@nanoctr.cn.
*E-mail: wgchu@nanoctr.cn

Notes

The authors declare no competing financial interest.

ACKNOWLEDGMENTS

This work is financially supported by the subproject "Exploration of novel cathode materials for lithium ion battery as highly efficient energy storage", the project "Design and Research on the Key Technology of Photovoltaic Demonstration Base", and the Knowledge Innovation Program of the Chinese Academy of Sciences, and the Strategic Priority Research Program of the Chinese Academy of Sciences, grant No. XDA09040101.

REFERENCES

(1) Padhi, K.; Nanjundaswamy, K. S.; Goodenough, J. B. Phospho-olivines as Positive-Electrode Materials for Rechargeable Lithium Batteries. *J. Electrochem. Soc.* **1997**, *144*, 1188−1194.

(2) Meethong, N.; Kao, Y. H.; Speakman, S. A.; Chiang, Y. M. Aliovalent Substitutions in Olivine Lithium Iron Phosphate and Impact on Structure and Properties. *Adv. Funct. Mater.* **2009**, *19*, 1060−1070.

(3) Prosini, P. P.; Lisi, M.; Zane, D.; Pasquali, M. Determination of the Chemical Diffusion Coefficient of Lithium in $LiFePO_4$. *Solid State Ionics* **2002**, *148*, 45−51.

(4) Amin, R.; Balaya, P.; Maier, J. Anisotropy of Electronic and Ionic Transport in $LiFePO_4$ Single Crystals. *Electrochem. Solid-State Lett.* **2007**, *10*, A13−A16.

(5) Chung, S. Y.; Bloking, J. T.; Chiang, Y. M. Electronically Conductive Phospho-Olivines as Lithium Storage Electrodes. *Nat. Mater.* **2002**, *1*, 123−128.

(6) Schougaard, S. B.; Breger, J.; Jiang, M.; Grey, C. P.; Goodenough, J. B. $LiNi_{0.5+\delta}Mn_{0.5-\delta}O_2$—A High-Rate, High-Capacity Cathode for Lithium Rechargeable Batteries. *Adv. Mater.* **2006**, *18*, 905−909.

(7) Croce, F.; Epifanio, A. D.; Hassoun, J.; Deptula, A.; Olczac, T.; Scrosati, B. A Novel Concept for the Synthesis of an Improved $LiFePO_4$ Lithium Battery Cathode. *Electrochem. Solid-State Lett.* **2002**, *5*, A47−A50.

(8) Ravet, N.; Chouinard, Y.; Magnan, J. F.; Besner, S.; Gauthier, M.; Armand, M. Electroactivity of Natural and Synthetic Triphylite. *J. Power Sources* **2001**, *97*−*98*, 503−507.

(9) Dominko, R.; Bele, M.; Gaberscek, M.; Remskar, M.; Hanzel, D.; Pejovnik, S.; Jamnik, J. Impact of the Carbon Coating Thickness on the Electrochemical Performance of $LiFePO_4$/C Composites. *J. Electrochem. Soc.* **2005**, *152*, A607−A610.

(10) Huang, H.; Yin, S. C.; Nazar, L. F. Approaching Theoretical Capacity of $LiFePO_4$ at Room Temperature at High Rates. *Electrochem. Solid-State Lett.* **2001**, *4*, A170−A172.

(11) Cui, G.; Hu, Y. S.; Zhi, L.; Wu, D.; Lieberwirth, I.; Maier, J.; Mullen, K. A One-Step Approach Towards Carbon-Encapsulated Hollow Tin Nanoparticles and Their Application in Lithium Batteries. *Small* **2007**, *3*, 2066−2069.

(12) Cui, G.; Gu, L.; Zhi, L.; Kaskhedikar, N.; van Aken, P. A.; Mullen, K.; Maier, J. A Germanium−Carbon Nanocomposite Material for Lithium Batteries. *Adv. Mater.* **2008**, *20*, 3079−3083.

(13) Delacourt, C.; Poizot, P.; Levasseur, S.; Masquelier, C. Size Effects on Carbon-Free $LiFePO_4$ Powders The Key to Superior Energy Density. *Electrochem. Solid-State Lett.* **2006**, *9*, A352−A355.

(14) Kim, D. H.; Kim, J. Synthesis of $LiFePO_4$ Nanoparticles in Polyol Medium and Their Electrochemical Properties. *Electrochem. Solid-State Lett.* **2006**, *9*, A439−A442.

(15) Wang, Y.; Wang, J.; Yang, J.; Nuli, Y. High-Rate $LiFePO_4$ Electrode Material Synthesized by a Novel Route from $FePO_4{\cdot}4H_2O$. *Adv. Funct. Mater.* **2006**, *16*, 2135−2140.

(16) Hanai, K.; Maruyama, T.; Imanishi, N.; Hirano, A.; Takeda, Y.; Yamamoto, O. Enhancement of Electrochemical Performance of Lithium Dry Polymer Battery with $LiFePO_4$/Carbon Composite cathode. *J. Power Sources* **2008**, *178*, 789−794.

(17) Doeff, M. M.; Wilcox, J. D.; Kostecki, R.; Lau, G. Optimization of Carbon Coatings on $LiFePO_4$. *J. Power Sources* **2006**, *163*, 180−184.

(18) Kadoma, Y.; Kim, J. M.; Abiko, K.; Ohtsuki, K.; Ui, K.; Kumagai, N. Optimization of Electrochemical Properties of $LiFePO_4$/C Prepared by an Aqueous Solution Method Using Sucrose. *Electrochim. Acta* **2010**, *55*, 1034−1041.

(19) Myung, S. T.; Komaba, S.; Hirosaki, N.; Yashiro, H.; Kumagai, N. Emulsion Drying Synthesis of Olivine $LiFePO_4$/C Composite and its Electrochemical Properties as Lithium Intercalation Material. *Electrochim. Acta* **2004**, *49*, 4213−4222.

(20) Hu, Y. S.; Guo, Y. G.; Dominko, R.; Gaberscek, M.; Jamnik, J.; Maier, J. Improved Electrode Performance of Porous $LiFePO_4$ Using RuO_2 as an Oxidic Nanoscale Interconnect. *Adv. Mater.* **2007**, *19*, 1963−1966.

(21) Wang, Y.; Wang, Y.; Hosono, E.; Wang, K.; Zhou, H. The Design of a $LiFePO_4$/Carbon Nanocomposite With a Core−Shell Structure and Its Synthesis by an In Situ Polymerization Restriction Method. *Angew. Chem., Int. Ed.* **2008**, *47*, 7461−7465.

(22) Li, X.; Wang, H.; Song, H.; Li, H.; Huang, J.; Yoon, S.; Kang, F. In-situ Preparation and Electrochemical Performance of an Urchin-like Carbon Nanofibers@$LiFePO_4$ Hybrid. *Int. J. Electrochem. Sci.* **2012**, *7*, 4397−4404.

(23) Uno, Y.; Tsujikawa, T.; Hirai, T. Electrochemical Properties of Helical Carbon Nanomaterials Formed on $LiCoO_2$ by Chemical Vapor Deposition. *J. Power Sources* **2010**, *195*, 354−357.

(24) Sun, X.; Li, J.; Shi, C.; Wang, Z.; Liu, E.; He, C.; Du, X.; Zhao, N. Enhanced Electrochemical Performance of $LiFePO_4$ Cathode with In-Situ Chemical Vapor Deposition Synthesized Carbon Nanotubes as Conductor. *J. Power Sources* **2012**, *220*, 264−268.

(25) Gong, Q.; He, Y.; Yang, Y.; Liao, X.; Ma, Z. Synthesis and Electrochemical Characterization of $LiFePO_4$/C-Polypyrrole Composite Prepared by a Simple Chemical Vapor Deposition Method. *J. Solid State Electrochem.* **2012**, *16*, 1383−1388.

(26) Wang, F.; Yang, J.; Gao, P.; NuLi, Y.; Wang, J. Morphology Regulation and Carbon Coating of $LiMnPO_4$ Cathode Material for Enhanced Electrochemical Performance. *J. Power Sources* **2011**, *196*, 10258−10262.

(27) Zhao, B.; Jiang, Y.; Zhang, H.; Tao, H.; Zhong, M.; Jiao, Z. Morphology and Electrical Properties of Carbon Coated $LiFePO_4$ Cathode Materials. *J. Power Sources* **2009**, *189*, 462−466.

(28) Tian, R. Y.; Liu, G. Y.; Liu, H. Q.; Zhang, L. N.; Gu, X. H.; Guo, Y. J.; Wang, H. F.; Sun, L. F.; Chu, W. G. Very High Power and Superior Rate Capability $LiFePO_4$ Nanorods Hydrothermally Synthesized Using Tetraglycol as Surfactant. *RSC Adv.* **2015**, *5*, 1859−1866.

(29) Wagemaker, M.; Ellis, B. L.; Lützenkirchen-Hecht, D.; Mulder, F. M.; Nazar, L. F. Proof of Supervalent Doping in Olivine $LiFePO_4$. *Chem. Mater.* **2008**, *20*, 6313−6315.

(30) Rehani, B.; Joshi, P. B.; Lad, K. N.; Pratap, A. Crystallite Size Estimation of Elemental and Composite Silver Nano-Powders Using XRD Principles. *Indian J. Pure Appl. Phys.* **2006**, *44*, 157−161.

(31) Morgan, D.; Van der Ven, A.; Ceder, G. Li Conductivity in Li_xMPO_4 (M = Mn, Fe, Co, Ni) Olivine Materials. *Electrochem. Solid-State Lett.* **2004**, *7*, A30−A32.

(32) Islam, M. S.; Driscoll, D. J.; Fisher, C. A. J.; Slater, P. R. Atomic-Scale Investigation of Defects, Dopants, and Lithium Transport in the

DOI: 10.1021/acsami.5b01891
ACS Appl. Mater. Interfaces 2015, 7, 11377−11386

$LiFePO_4$ Olivine-Type Battery Material. *Chem. Mater.* **2005**, *17*, 5085−5092.
(33) Fisher, C. A. J.; Islam, M. S. Surface Structures and Crystal Morphologies of $LiFePO_4$: Relevance to Electrochemical Behaviour. *J. Mater. Chem.* **2008**, *18*, 1209−1215.
(34) Wang, L.; He, X. M.; Sun, W. T.; Wang, J. L.; Li, Y. D.; Fan, S. S. Crystal Orientation Tuning of $LiFePO_4$ Nanoplates for High Rate Lithium Battery Cathode Materials. *Nano Lett.* **2012**, *12*, 5632−5636.
(35) Dominko, R.; Goupil, J. M.; Bele, M.; Gaberscek, M.; Remskar, M.; Hanzel, D.; Jamnik, J. Impact of $LiFePO_4$/C Composites Porosity on Their Electrochemical Performance. *J. Electrochem. Soc.* **2005**, *152*, A858−A863.
(36) Qian, J. F.; Zhou, M.; Cao, Y. L.; Ai, X. P.; Yang, H. X. Template-Free Hydrothermal Synthesis of Nanoembossed Mesoporous $LiFePO_4$ Microspheres for High-Performance Lithium-Ion Batteries. *J. Phys. Chem. C* **2010**, *114*, 3477−3482.
(37) Wi, S. G.; Nam, S.; Oh, Y. H.; Kim, J. M.; Choi, H.; Hong, S. J.; Byun, S. J.; Kang, D. J.; Choi, K.; Ahn, Y. H.; Kim, S.; Park, B. Facile Synthesis of Porous-Carbon/$LiFePO_4$ Nanocomposites. *J. Nanopart. Res.* **2012**, *14*, 1327−1335.
(38) Liu, Q. B.; Liao, S. J.; Song, H. Y.; Liang, Z. X. High-Performance $LiFePO_4$/C Materials: Effect of Carbon Source on Microstructure and Performance. *J. Power Sources* **2012**, *211*, 52−58.
(39) Thomsen, C.; Reich, S. Double Resonant Raman Scattering in Graphite. *Phys. Rev. Lett.* **2000**, *85*, 5214−5217.
(40) Saito, R.; Jorio, A.; Filho, A. G. S.; Dresselhaus, G.; Dresselhaus, M. S.; Pimenta, M. A. Probing Phonon Dispersion Relations of Graphite by Double Resonance Raman Scattering. *Phys. Rev. Lett.* **2002**, *88*, No. 027401.
(41) Tuinstra, F.; Koenig, J. L. Raman Spectrum of Graphite. *J. Chem. Phys.* **1970**, *53*, 1126−1130.
(42) Lespade, P.; Marchand, A.; Couzi, M.; Cruege, F. Caracterisation De Materiaux Carbones Par Microspectrometrie Raman. *Carbon* **1984**, *22*, 375−385.
(43) Beyssac, O.; Rouzaud, J. N.; Goffe, B.; Brunet, F.; Chopin, C. Graphitization in a High-Pressure, Low-Temperature Metamorphic Gradient: A Raman Microspectroscopy and HRTEM Study. *Contrib. Mineral. Petrol.* **2002**, *143*, 19−31.
(44) Doeff, M. M.; Hu, Y. Q.; McLarnon, F.; Kostecki, R. Effect of Surface Carbon Structure on the Electrochemical Performance of $LiFePO_4$. *Electrochem. Solid-State Lett.* **2003**, *6*, A207−A209.
(45) Wilcox, J. D.; Doeff, M. M.; Marcinek, M.; Kostecki, R. Factors Influencing the Quality of Carbon Coatings on $LiFePO_4$. *J. Electrochem. Soc.* **2007**, *154*, A389−A395.
(46) Matthews, M. J.; Pimenta, M. A.; Dreesselhaus, G.; Dreesselhaus, M. S.; Endo, M. Origin of Dispersive Effects of the Raman D Band in Carbon materials. *Phys. Rev. B* **1999**, *59*, R6585−R6588.
(47) Maccario, M.; Croguennec, L.; Desbat, B.; Couzi, M.; Cras, F. L.; Servant, L. Raman and FTIR Spectroscopy Investigations of Carbon-Coated Li_xFePO_4 Materials. *J. Electrochem. Soc.* **2008**, *155*, A879−A886.
(48) Zhou, X. F.; Wang, F.; Zhu, Y. M.; Liu, Z. P. Graphene-Modified $LiFePO_4$ Cathode Materials for High Power Lithium Ion Batteries. *J. Mater. Chem. A* **2011**, *21*, 3353−3358.
(49) Hu, L. H.; Wu, F. Y.; Lin, C. T.; Khlobystov, A. N.; Li, L. J. Graphene-Modified $LiFePO_4$ Cathode for Lithium Ion Battery Beyond Theoretical Capacity. *Nat. Commun.* **2013**, *4*, 1−7.
(50) Kang, B.; Ceder, G. Battery Materials for Ultrafast Charging and Discharging. *Nature* **2009**, *458*, 190−193.
(51) Wu, X. L.; Guo, Y. G.; Su, J.; Xiong, J. W.; Zhang, Y. L.; Wan, L. J. Carbon-Nanotube-Decorated Nano-$LiFePO_4$@C Cathode Material with Superior High-Rate and Low-Temperature Performances for Lithium-Ion Batteries. *Adv. Energy Mater.* **2013**, *3*, 1155−1160.
(52) Liu, X. M.; Yan, P.; Xie, Y. Y.; Yang, H.; Shen, X. D.; Ma, Z. F. Synthesis of Superior Fast Charging−Discharging Nano-$LiFePO_4$/C from Nano-$FePO_4$ Generated Using a Confined Area Impinging Jet Reactor Approach. *Chem. Commun.* **2013**, *49*, 5396−5398.
(53) Rui, X. H.; Zhao, X. X.; Lu, Z. Y.; Tan, H. T.; Sim, D. H.; Hong, H. H.; Yazami, R.; Lim, T. M.; Yan, Q. Y. Olivine-Type Nanosheets for Lithium Ion Battery Cathodes. *ACS Nano* **2013**, *7*, 5637−5646.
(54) Zhang, J. L.; Wang, J.; Liu, Y. Y.; Ning, N.; Gu, J. J.; Feng, Y.; Li, W. High-Performance Lithium Iron Phosphate with Phosphorus-Doped Carbon Layers for Lithium Ion Batteries. *J. Mater. Chem. A* **2015**, *3*, 2043−2049.
(55) Wang, J. J.; Sun, X. L. Understanding and Recent Development of Carbon Coating on $LiFePO_4$ Cathode Materials for Lithium-Ion Batteries. *Energy Environ. Sci.* **2012**, *5*, 5163−5185.
(56) Shu, H. B.; Wang, X. Y.; Wen, W. C.; Liang, Q. Q.; Yang, X. K.; Wei, Q. L.; Hu, B. N.; Liu, L.; Liu, X.; Song, Y. F.; Zho, M.; Bai, Y. S.; Jiang, L. L.; Chen, M. F.; Yang, S. Y.; Tan, J. L.; Liao, Y. Q.; Jiang, H. M. Effective Enhancement of Electrochemical Properties for $LiFePO_4$/C Cathode Materials by Na and Ti Co-Doping. *Electrochim. Acta* **2013**, *89*, 479−487.
(57) Wang, Y.; Cao, G. Z. Developments in Nanostructured Cathode Materials for High-Performance Lithium-Ion Batteries. *Adv. Mater.* **2008**, *20*, 2251−2269.
(58) Chen, J.; Zou, Y. C.; Zhang, F.; Zhang, Y. C.; Guo, F. F.; Li, G. D. Superior Electrode Performance of $LiFePO_4$/C Composite Prepared by an In Situ Polymerization Restriction Method. *J. Alloys Compd.* **2013**, *563*, 264−268.
(59) Li, J.; Zhang, L.; Zhang, L. F.; Hao, W. W.; Wang, H. B.; Ou, Q. T.; Zheng, H. H. In-Situ Growth of Graphene Decorations for High-Performance $LiFePO_4$ Cathode through Solid-State Reaction. *J. Power Sources* **2014**, *249*, 311−319.
(60) Wang, B.; Abdulla, W.; Wang, D. L.; Zhao, X. S. A Three-Dimensional Porous $LiFePO_4$ Cathode Material Modified with a Nitrogen-Doped Graphene Aerogel for High-Power Lithium Ion Batteries. *Energy Environ. Sci.* **2015**, *8*, 869−875.
(61) Churikova, A. V.; Ivanishcheva, A. V.; Ivanishchevaa, I. A.; Sychevaa, V. O.; Khasanovab, N. R.; Antipovb, E. V. Determination of Lithium Diffusion Coefficient in $LiFePO_4$ Electrode by Galvanostatic and Potentiostatic Intermittent Titration Techniques. *Electrochim. Acta* **2010**, *55*, 2939−2950.
(62) Zhang, X. Y.; Hulzen, M.; Singh, D. P.; Brownrigg, A.; Wright, J. P.; Dijk, V. H.; Wagemaker, M. Rate-Induced Solubility and Suppression of the First-Order Phase Transition in Olivine $LiFePO_4$. *Nanolett.* **2014**, *14*, 2279−285.
(63) Wang, Y.; Mei, R.; Yang, X. Enhanced Electrochemical Properties of $LiFePO_4$/C Synthesized with Two Kinds of Carbon Sources, PEG-4000 (Organic), and Super p (Inorganic). *Ceram. Int.* **2014**, *40*, 8439−8444.
(64) Chen, Z. Y.; Zhu, H. L.; Ji, S.; Fakir, R.; Linkov, V. Influence of Carbon Sources on Electrochemical Performances of $LiFePO_4$/C Composites. *Solid State Ionics* **2008**, *179*, 1810−1815.
(65) Choy, K. L. Chemical Vapour Deposition of Coatings. *Prog. Mater. Sci.* **2003**, *48*, 57−170.

DOI: 10.1021/acsami.5b01891
ACS Appl. Mater. Interfaces 2015, 7, 11377−11386